X-ray and γ-ray spectroscopy using a 2 × 2 GaAs p+-i-n+ diode array

Article (Accepted Version)

X-ray and γ-ray spectroscopy using a 2 × 2 GaAs p^+-i-n^+ diode array

G. Lioliou[a] and A. M. Barnett
Space Research Group, School of Mathematical and Physical Sciences, University of Sussex, Falmer, Brighton BN1 9QT, UK

Abstract

A GaAs 2 × 2 pixel monolithic X-ray detector array was fabricated from material grown by metalorganic vapour phase epitaxy. Each pixel was a 200 μm × 200 μm square mesa p^+-i-n^+ photodiode with a 10 μm thick i layer. The array was electrically characterized and then each pixel was connected to the input of a custom-made, low noise, charge-sensitive preamplifier in turn. ^{55}Fe X-ray, ^{109}Cd X-ray and γ-ray, and ^{241}Am X-ray and γ-ray spectra were accumulated at 20 °C. Following this, the spectroscopic response of one of the pixels was investigated at temperatures ≤ 100 °C. With both the preamplifier and detector array operated at 100 °C, the energy resolution (Full Width at Half Maximum) was 1.61 keV ± 0.04 keV at 5.9 keV, 1.63 keV ± 0.06 keV at 22.16 keV, and 1.65 keV ± 0.08 keV at 59.54 keV. The results suggested that the pixels did not suffer from incomplete charge collection. The energy resolution achieved is the best reported so far for GaAs spectrometers at such high temperatures.

Keywords: GaAs; X-ray spectroscopy; γ-ray spectroscopy; pixel detector; array

1. Introduction

Imaging X-ray spectroscopy is a powerful technique in space science. From the Chandra X-ray Observatory [1] and XMM-Newton [2], to Swift [3] and Suzaku [4], X-ray imaging spectroscopy has enabled high resolution studies of the structure of X-ray sources (e.g. supernova remnants and astrophysical jets), galaxies, and clusters of galaxies, as well as determination of the position of γ-ray bursts. The X-ray imaging spectrometer in XMM-Newton, for example, consists of Si CCD arrays (12 subunits of 200 × 68 pixels each) which have good detection efficiency for photons of energy up to 10 keV, and a pre-launch energy resolution (Full Width at Half Maximum, *FWHM*) of 137 eV at 5.9 keV when operated at -100 °C [5]. X-ray imaging spectrometers can also be used for analysis of planetary surfaces (planets, moons, comets, and asteroids), with a notable example being the Mercury Imaging X-ray Spectrometer (MIXS) on-board BepiColombo [6]. MIXS will measure X-ray fluorescence from the surface of Mercury at energies between 0.5 keV and 7.5 keV in order to map the elemental surface composition of the planet. MIXS uses microchannel plate X-ray optics and Si Macropixel DEPFET detector arrays [7]; the energy resolution of the DEPFET detectors is expected to be 100 eV *FWHM* at 1 keV at the start of operations, degrading through the mission's lifetime due to radiation damage.

In applications such as X-ray astronomy which commonly experience a relative paucity of photons, the use of Si for imaging X-ray spectroscopy is limited to soft X-rays as a consequence of the relatively low linear absorption coefficients of the material at X-ray energies [8]. Instead, high *Z* compound semiconductor detectors, which have larger linear absorption coefficients, such as CdZnTe and GaAs, are preferable for detectors which need to have good detection efficiency at higher photon energies (typically ≳ 10 keV). The importance of excellent detection efficiencies for detectors used in imaging in low flux environments is intensified further for imaging (cf. non-imaging) applications: when imaging, the total photon flux available is necessarily spread across the detector pixel array thus reducing the number of photons available per pixel, even in coded aperture instruments. In contrast, in non-imaging applications all photons can be focused onto a single pixel.

[a] Corresponding author. Tel.: +44 (0) 1273 872568. E-mail address: G.Lioliou@sussex.ac.uk

CdZnTe pixel detectors were employed in Swift's Burst Alert Telescope (BAT) and Astrosat's Cadmium-Zinc-Telluride Imager (CZTI) [9]. The imaging capabilities of BAT were achieved using a coded aperture mask [10]; pre-launch, BAT had an energy resolution of 6.2 keV at 122 keV when operated at 20 °C (the nominal operating temperature while on orbit). CZTI has an energy resolution of ~8 keV at 100 keV when operated at 0 °C. The best energy resolution achieved at room temperature with $Cd_{1-x}Zn_xTe$ detectors to date was with a CdTe pixel detector coupled to an ultra low noise CMOS charge-sensitive preamplifier; a *FWHM* of 843 eV at 59.54 keV was reported [11]; the detector was reported to suffer from charge trapping, leading to incomplete charge collection noise [11] [12]. $Cd_{1-x}Zn_xTe$ detectors can also suffer from degradation in spectral response (deterioration of energy resolution and peak shift to lower channel number) due to Te inclusions and polarization effects [13].

An alternative to $Cd_{1-x}Zn_xTe$ for low and medium energy X-ray and γ-ray imaging spectroscopy is GaAs [14]. The 1.42 eV bandgap of GaAs at 20 °C [15] (cf. 1.12 eV for Si [16]; 1.44 eV for CdTe [17]) allows uncooled operation of GaAs detectors at high temperatures (> 20 °C). The average electron-hole pair creation energy, ω, and Fano factor, F, of GaAs, 4.184 eV at 5.9 keV [15] and 0.12 [18], respectively, results in charge carrier creation statistics and Fano limited spectroscopic resolutions similar to Si (ω = 3.62 eV [19], F = 0.118 [20]), and slightly better than those of $Cd_{1-x}Zn_xTe$ (ω = 4.43 eV for x = 0 and ω = 4.6 eV for x = 0.1 [17], $0.084 \leq F \leq 0.24$ [11]). Furthermore, the high radiation resistance of GaAs [21] makes it a suitable choice in space environments with intense radiation.

However, whilst GaAs has greater linear X-ray absorption coefficients than Si (e.g. 10.84 cm^{-1} c.f. 0.75 cm^{-1} at 60 keV [8]), $Cd_{1-x}Zn_xTe$ has greater linear X-ray absorption coefficients than GaAs (ranging from 30.36 cm^{-1} to 37.81 cm^{-1} at 60 keV, dependent on x [8]. Thus, whilst GaAs can provide better quantum detection efficiencies per unit thickness than Si, the detection efficiency per unit thickness of GaAs is lower than that of $Cd_{1-x}Zn_xTe$, particularly at high photon energies. Furthermore, at present, GaAs structures are not commonly grown as thick as CdZnTe structures (e.g. 5 mm in CZTI [22]). As such, GaAs fills a niche for X-ray and γ-ray imaging spectroscopy at modest X-ray and γ-ray photon energies. GaAs extends the efficiently detectable photon energy range beyond that of Si. However, the expectation would remain that CdZnTe detectors would still be used for the highest energy photons. Thus, a combination of GaAs and CdZnTe detectors could be used instead of Si detectors to cover a wide energy range with good energy resolution in a number of space and terrestrial applications where operation is required in high temperature and intense radiation environments.

The best experimental results reported to date for GaAs pixel detectors are for pixels with structures including an ultrapure epitaxial planar layer, when coupled to ultra low noise preamplifier electronics [14] [23]. Initially, Owens et al. [14] reported a 5 × 5 GaAs diode array structure (200 μm × 200 μm pixel size). It included a 40 μm thick epitaxial i layer, forming a p^+-i-n^+ structure, Au/Pt/Ti Schottky contacts at the p^+ layer, and a guard ring surrounding the pixel array structure. Two of the pixels were investigated; an energy resolution (*FWHM*) of 266 eV at 5.9 keV at room temperature was reported. Following this, larger devices (250 μm × 250 μm) with a thicker epilayer (325 μm) and similar structure to the previously reported detector (by Owes et al. [14]), in a 32 × 32 pixel array, have been reported [23]. Four of the pixels were investigated; an energy resolution of 300 eV *FWHM* at 5.9 keV and 650 eV *FWHM* at 59.54 keV at room temperature was achieved [23].

In this article, a monolithic (single die) GaAs 2 × 2 pixel array of square mesa photodiodes is investigated for its X-ray and γ-ray spectroscopic performance; although this detector is smaller and thinner compared to the previous reported GaAs pixel detectors [14] [23], all four pixels were characterized and the detector was subjected to a temperature up to 100 °C. It was electrically

characterized at 20 °C, while one of the pixels was investigated up to 100 °C; the dark currents and capacitances of each pixel were measured and the important electrical parameters were calculated. Following this, the pixel array was coupled to a custom-made, charge-sensitive preamplifier, and ^{55}Fe X-ray, ^{109}Cd X-ray and γ-ray, and ^{241}Am X-ray and γ-ray spectra were accumulated with each pixel, thus covering an energy range of 5.9 keV to 88 keV. The spectroscopic performance for each of the four pixels was investigated at 20 °C, and then one of the pixels was further characterized at temperatures ≤ 100 °C.

2. Array structure

A GaAs p^+-i-n^+ structure was grown by metalorganic vapour phase epitaxy (MOVPE) on a commercial 2 inch GaAs n^+ substrate. The p^+ layer (thickness of 0.5 µm) was doped with C at a density of 2×10^{18} cm^{-3}. The n^+ layer (thickness of 1 µm) was doped with Si at a density of 2×10^{18} cm^{-3}. The unintentionally doped i layer was 10 µm thick. A GaAs 2 × 2 pixel array of square mesa diodes (each 200 µm × 200 µm in size, with a 10 µm radius at each corner to prevent corner breakdown and 15 µm between adjacent pixels) was wet etched using a 1:1:1 H_3PO_4:H_2O_2:H_2O solution followed by 10 s in a 1:8:80 H_2SO_4:H_2O_2:H_2O solution. Top Ohmic contacts (covering 50% of the top face of each pixel) were deposited consisting of 20 nm Ti and 200 nm of Au. A planar common bottom contact was formed with 20 nm of InGe and 200 nm of Au. **Figure 1** shows the layer structure (cross section) of each pixel and the layout of the array. In order to identify each pixel of the array they were named D1, D2, D3, and D4.

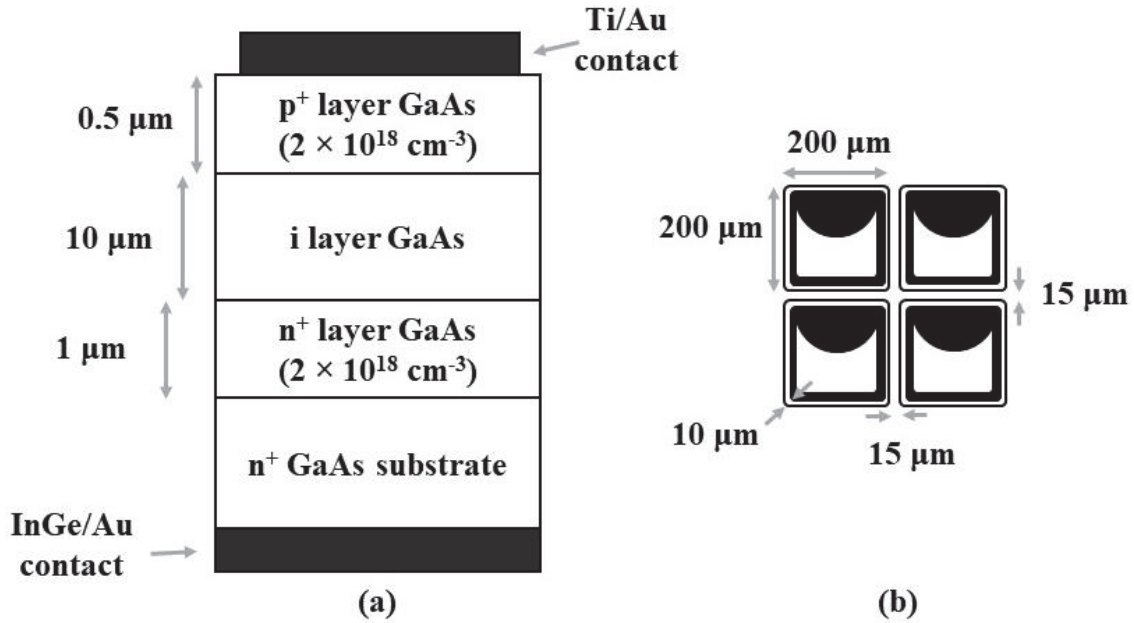

Figure 1. Illustrative (a) layer structure of each pixel and (b) layout of the 2 × 2 GaAs photodiode array (not to scale). The shaded area represents the Ohmic contacts. D1 is the top left, D2 is the top right, D3 is the bottom left, D4 is the bottom right.

3. Dark current measurements of GaAs pixel detectors

The dark current of each pixel was measured as a function of applied forward bias (up to 1 V) and applied reverse bias (up to -50 V) in order to extract the saturation current, I_0, ideality factor, n, leakage current noise contribution (to the spectrometer's achieved energy resolution), and to identify the dominant current mechanism.

The array was installed in a light tight Al enclosure; temperature control was achieved by using a TAS Micro LT climatic cabinet. The bias was applied and the current was measured, for each pixel in turn, using a Keithley 6487 Picoammeter/Voltage Source. Initially, the dark current as a function of applied forward and reverse bias of each GaAs pixel was measured at 20 °C, and then the dark current of D1 was measured as a function of temperature (100 °C to 20 °C, with a -20 °C step). The leakage current associated with the TO-5 package of the array was also measured as a function of bias and temperature, the package leakage current was then separated from the total measured dark current in the analysis. The dark current measured at 20 °C as a function of applied forward and reverse bias for each of the four pixels can be seen in **Fig. 2**.

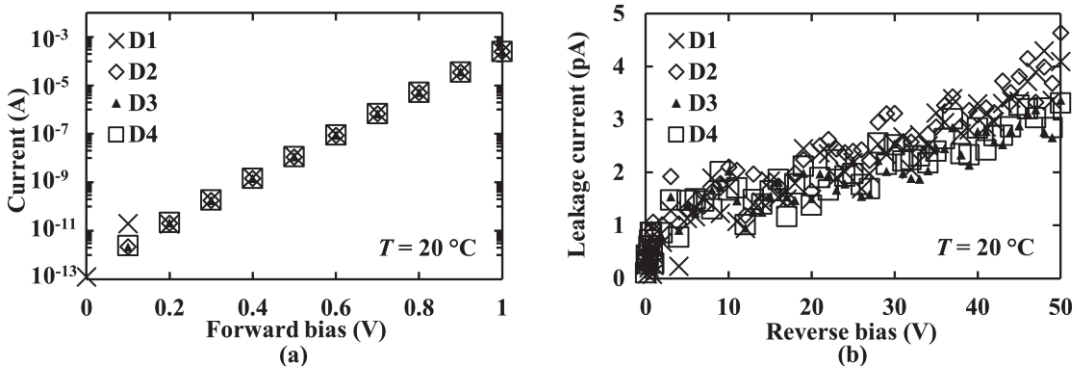

Figure 2. Dark current as a function of (a) forward and (b) reverse bias of the four pixels at 20 °C.

The saturation current and the ideality factor of the GaAs p^+-i-n^+ diodes were extracted from the semi-logarithmic current as a function of applied forward bias data. A mean saturation current of 350 fA ± 10 fA and a mean ideality factor of 1.90 ± 0.01 were calculated for all diodes at 20 °C. The stated rms errors were the root mean square of the deviations from the mean. The variance of the extracted saturation current and ideality factor among the diodes of the array was within the uncertainty arising from the accuracy of the Keithley 6487 Picoammeter/Voltage Source for the forward biased current measurements. Ideality factor values close to 2 suggested that the recombination current dominated over the diffusion current when the pixels were forward biased [24]. Similar leakage currents were measured for all four pixels; a mean leakage current of 3.9 pA ± 0.5 pA was measured at the maximum applied reverse bias (-50 V) at 20 °C. The key parameters for each pixel are summarised in **Table 1**.

The measured current of D1 as a function of applied forward and reverse bias, and temperature, T, 20 °C ≤ T ≤ 100 °C, can be seen in **Fig. 3**. The saturation current decreased from 290 pA ± 30 pA at 100 °C to 330 fA ± 40 fA at 20 °C. The ideality factor remained stable within uncertainties (1.87 ± 0.02 at 100 °C; 1.89 ± 0.02 at 20 °C). The uncertainties in the saturation current and the ideality factor were related to the standard deviation of the gradient and the intercept point of the line of best fit calculated for the semi-logarithmic current as a function of applied forward bias, using linear least squares fitting.

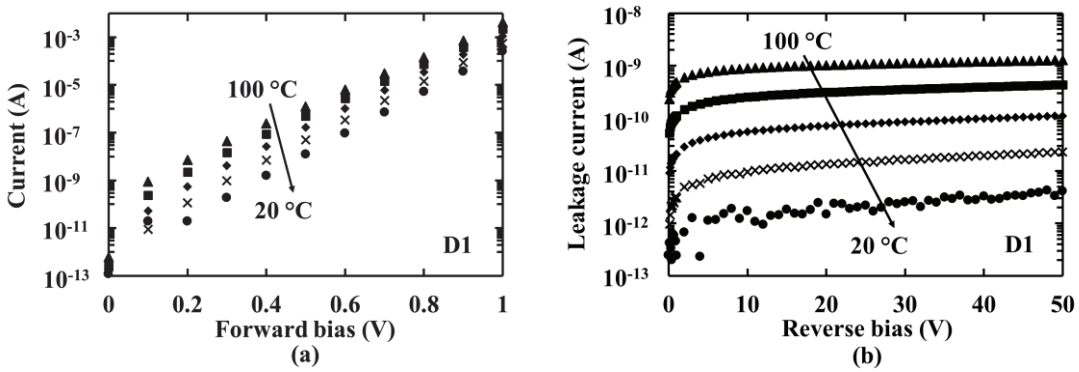

Figure 3. Dark current as a function of (a) forward and (b) reverse bias of D1 within the temperature range 100 °C to 20 °C.

The leakage current of D1 at -50 V reverse bias (50 kV/cm electric field strength), decreased from 1.281 nA ± 0.006 nA at 100 °C to 4.1 pA ± 0.4 pA at 20 °C. Assuming the leakage current originated from the bulk of the GaAs diode (i.e. excluding contributions from the surface), the leakage current density as a function of temperature can be calculated by dividing the measured leakage current by the area of the diode (0.0004 cm^2) at each applied electric field. At highest electric field strength (50 kV/cm), the leakage current density decreased exponentially with decreasing temperature, from 3.20 $\mu A/cm^2$ ± 0.02 $\mu A/cm^2$ at 100 °C to 10 nA/cm^2 ± 1 nA/cm^2 at 20 °C. The line of best fit was calculated for the logarithm of the leakage current at -50 V reverse bias as a function of temperature using linear least squares fitting; the gradient of the line was 0.072 $°C^{-1}$ ± 0.004 $°C^{-1}$. The leakage current density measured here is better (lower) than that reported previously for a circular (200 μm diameter, 10 μm i layer thick) mesa GaAs p^+-i-n^+ X-ray detector (5.14 $\mu A/cm^2$ ± 0.02 $\mu A/cm^2$ at 100 °C and 50 kV/cm electric field strength) [25].

The dominant current mechanism when a photodiode is reverse biased can be determined by plotting the logarithm of the photodiode's leakage current density as a function of 1/kT, where k is the Boltzmann constant and T is the temperature in Kelvin. A gradient of -E_G indicates diffusion current; whereas a gradient of -E_G/2 indicates generation current [26]. Using this method for D1 reverse biased at -50 V, suggested that generation current dominated within the investigated temperature range; the gradient was -0.68 ± 0.01, thus ≈ -E_G/2. Where recombination current dominates in forward bias, high recombination rates are also exhibited in reverse bias, as is the case with D1 [26].

Table 1. A summary of the saturation currents, ideality factors, and leakage currents at -50 V applied bias, for all four pixels at 20 °C.

Pixel	Saturation current (fA)	Ideality factor	Leakage current at -50 V (pA)
D1	330 ± 40	1.89 ± 0.02	4.1 ± 0.4
D2	340 ± 20	1.91 ± 0.01	4.6 ± 0.4
D3	350 ± 20	1.91 ± 0.01	3.4 ± 0.4
D4	360 ± 20	1.91 ± 0.01	3.3 ± 0.4

4. Dark capacitance measurements of GaAs pixel detectors

The depletion layer width and the effective carrier concentration in the i layer of all four pixels were calculated from capacitance measurements as functions of applied reverse bias, up to -50 V.

The array was installed in a light tight Al enclosure, inside a TAS Micro LT climatic cabinet for temperature control, as per the dark current measurements. The bias was applied using a Keithley 6487 Picoammeter/Voltage Source and the capacitance was measured using an HP Multi Frequency LCR meter with a 50 mV rms magnitude and 1 MHz frequency test signal. Initially, the capacitance of each pixel (packaged diode) was measured at 20 °C, and then the capacitance of D1 was measured as a function of temperature, (100 °C to 20 °C, with a -20 °C step). The capacitance of the package was also estimated; the capacitance between an empty pin and the package's common pin was measured as a function of temperature (e.g. 0.65 pF at 20 °C) and subtracted from the total measured capacitance of the packaged diodes, to result to the depletion layer capacitance. The capacitance between multiple empty pins and the package's common pin was measured at 20 °C, to determine the uncertainty associated with the measurement of the capacitance of the package (± 0.09 pF). The uncertainty associated with the reported depletion layer capacitances for each pixel was estimated to be ± 0.1 pF, whereas the uncertainties for the reported capacitance variations with applied reverse bias and temperature, which resulted from a single set of measurements taken at the same conditions (i.e. no interconnections were changed), was estimated to be ± 0.006 pF (proportional to the value of the corresponding measured capacitance). The depletion layer capacitance for each of the four pixels at 20 °C can be seen in **Fig. 4**.

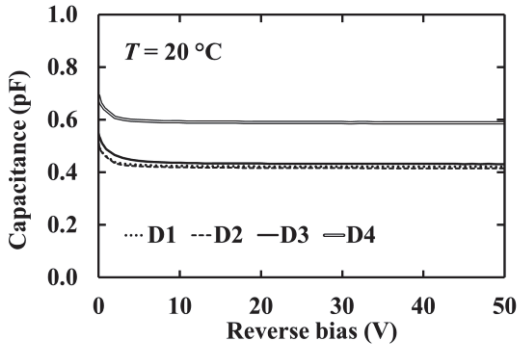

Figure 4. Capacitance as a function of reverse bias of the four pixels, at 20 °C.

The depletion layer capacitances (± 0.1 pF in each case) of each pixel were 0.4 pF for D1 – D3 and 0.6 pF for D4, at -50 V applied reverse bias and 20 °C. The depletion layer capacitance for all four pixels decreased as the applied reverse bias increased (in magnitude) from 0 V to -10 V, and remained stable for further increases of the bias. This suggested that the diodes were fully depleted at -10 V reverse bias. The depletion layer width of all four pixels was calculated from the measured depletion layer capacitance assuming they may be approximated as parallel plate capacitors [24]. It was 11 μm ± 3 μm for D1 – D3, whereas a depletion layer width of 8 μm ± 1 μm was calculated for D4, at the maximum applied reverse bias (-50 V). The thinner calculated depletion width of D4 cf. the rest of the pixels was unlikely to have been real (e.g. resulting from variations in the i layer thickness), instead it was attributed to D4 having a higher packaging capacitance than was estimated (0.65 pF ± 0.09 pF). If, instead, a 0.75 pF packaging capacitance was assumed for D4, the pixel's depletion width would have been calculated to be 9 μm ± 2 μm, consistent with the expected i layer thickness and identical to the other pixels. Such small variations in the packaging capacitance for devices connected to different pins of the package are consistent with previous measurements of the packaging capacitances associated TO-5 cans; variations in packaging capacitance of ± 0.1 pF have been observed previously. The variation of the depletion width of all four pixels at three applied biases can be seen in **Table 2**. The effective carrier concentration within the i layer, which follows the doping profile of the intrinsic layer providing that the doping profile does not have a spatial variation over distances less than a Debye length, was extracted from the capacitance measurements for all four pixels using the differential capacitance profiling method [24]. The measured effective carrier concentration within the i layer for all four pixels is shown in **Table 2**.

The effect of temperature on the depletion layer capacitance and the depletion layer width of D1 was investigated. The depletion layer capacitance of D1 as a function of applied reverse bias within the temperature range 100 °C to 20 °C can be seen in **Fig. 5 (a)**. It decreased from 0.562 pF at 100 °C to 0.508 pF at 20 °C at 0 V, and from 0.425 pF at 100 °C to 0.421 pF at 20 °C at -50 V reverse bias (in each case the uncertainty associated with the stated capacitances was ± 0.006 pF). The calculated depletion layer width of D1 as a function of applied reverse bias at the maximum and minimum temperatures, can be seen in **Fig. 5 (b)**.

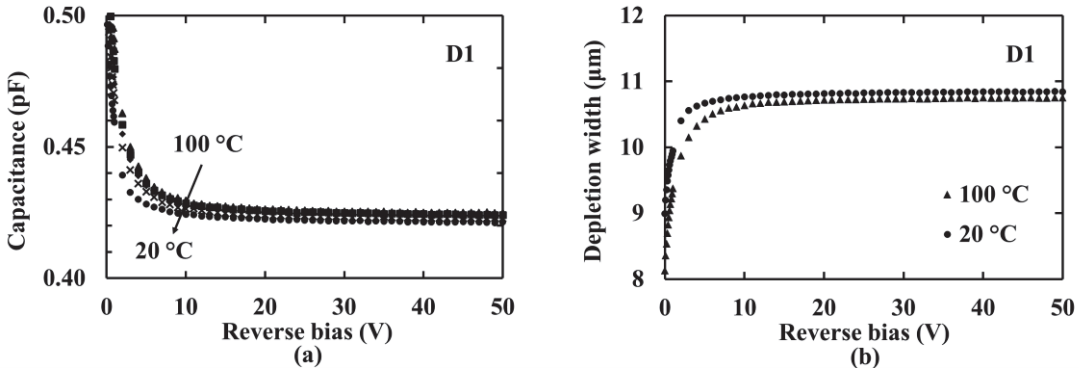

Figure 5. (a) Capacitance within the temperature range 100 °C to 20 °C and (b) calculated depletion layer width at 100 °C (filled triangles) and 20 °C (filled circles), as a function of applied reverse bias of D1.

The depletion layer width of the pixel increased from 8.13 μm ± 0.08 μm at 0 V to 10.8 μm ± 0.2 μm at -50 V reverse bias at 100 °C and from 9.0 μm ± 0.1 μm at 0 V to 10.8 μm ± 0.2 μm at -50 V reverse bias at 20 °C. It can be seen that the depletion width at low applied reverse biases was temperature dependent, whereas the depletion width at high applied reverse biases was temperature invariant, within uncertainties. The possible presence of a thin region around the depletion layer with non-ionised dopants at low temperatures, which were ionised at high temperatures, can explain the observed limited depletion layer width when no bias was applied at 100 °C, compared to the depletion layer width at 20 °C. The invariant depletion layer width with temperature at high reverse bias was attributed to the ratio between the thickness of this this region and the depletion layer being lower for high reverse biases compared to low reverse biases. Although D1 was fully depleted at -10 V applied reverse bias, it was found to be almost fully depleted at -5 V; the i layer was 97 % depleted and 98 % depleted at -5 V, at 100 °C and 20 °C, respectively.

The effective carrier concentration was calculated at distances > 8 μm below the p^+-i junction at 100 °C, and > 9 μm below the p^+-i junction at 20 °C; these can be seen in **Fig. 6**. The effective carrier concentration of D1 was 4×10^{13} cm^{-3} ± 2×10^{13} cm^{-3} at 8.13 μm ± 0.08 μm below the p^+-i junction at 100 °C, whereas the same effective carrier concentration was calculated at 20 °C (= 4×10^{13} cm^{-3} ± 3×10^{13} cm^{-3}) at 9.0 μm ± 0.1 μm bellow the p^+-i junction. Non-ionized dopants in a layer at the i-n^+ interface at 20 °C, which were ionized at 100 °C, may explain the difference between the effective doping concentration at these two temperatures. The relatively low effective doping concentration within the i layer (~ 10^{13} cm^{-3}) allowed the full depletion of D1 at -10 V applied reverse bias; a previously reported GaAs device with a thicker epilayer had a measured doping concentration of 1.5×10^{14} cm^{-3}; this set a limit of 32 μm to the depletion width at -100 V applied reverse bias [27].

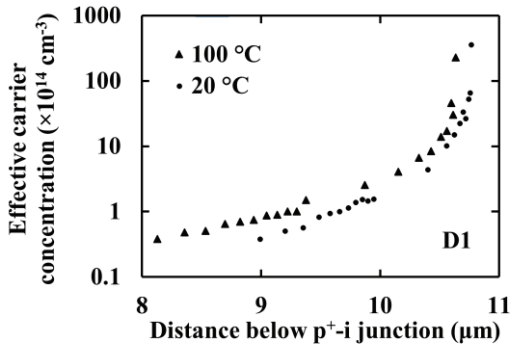

Figure 6. Effective carrier concentration for D1 as calculated at 100 °C (filled triangles) and 20 °C (filled circles).

Table 2. A summary of the depletion layer width at 0 V, -10 V, and -50 V applied reverse bias and the effective carrier concentration within the i layer, for all four pixels at 20 °C. The stated uncertainties resulted from the uncertainty (± 0.006 pF) of the capacitance measurements made as a function of applied reverse bias.

Pixel	Depletion width (μm)			Effective carrier conc. (× 10^{14} cm^{-3}) within i layer
	0 V	-10 V	-50 V	
D1	9.0 ± 0.1	10.8 ± 0.1	10.8 ± 0.1	0.4 ± 0.3
D2	9.0 ± 0.1	10.9 ± 0.1	11.0 ± 0.2	0.4 ± 0.3
D3	8.31 ± 0.09	10.5 ± 0.1	10.6 ± 0.1	0.3 ± 0.2
D4	6.61 ± 0.06	7.71 ± 0.08	7.77 ± 0.08	0.8 ± 0.5

5. X-ray and γ-ray spectroscopic measurements

5.1. Experimental procedures

X-ray and γ-ray spectra were accumulated using all four pixels in order to characterize their detection performance at 20 °C. Following investigation of the whole array at 20 °C, one representative pixel (D1) was investigated at higher temperatures (100 °C to 20 °C, with a -20 °C step).

Each pixel was connected, in turn, to the input of a custom-made, single-channel, charge-sensitive preamplifier. The charge-sensitive preamplifier was of a feedback-resistorless design; eliminating the feedback resistor, and any other external circuity to reset the preamplifier, reduced the noise of the spectroscopic system [28]. The input transistor of the charge-sensitive preamplifier, an InterFET 2N4416 JFET, was forced to operate with its gate-to-source junction slightly forward biased. The array and the preamplifier were installed inside a TAS Micro LT climatic cabinet with a dry environment, for temperature control. The preamplifier's output was connected to an Ortec 572A shaping amplifier, and the shaping amplifier's output was then digitized with an Ortec EASYMCA 8k multichannel analyser (MCA).

^{55}Fe X-ray spectra, ^{109}Cd X-ray and γ-ray spectra, ^{241}Am X-ray and γ-ray spectra, were accumulated. The ^{55}Fe X-ray spectra were accumulated as a function of applied reverse bias (0 V, -5 V, and -50 V) at all available shaping times (0.5 μs, 1 μs, 2 μs, 3 μs, 6 μs, 10 μs), to allow insight into the noise components of each pixel's spectroscopic system. However, the ^{109}Cd and ^{241}Am X-ray and γ-ray spectra were accumulated at only the optimum shaping time and reverse bias (i.e. those which gave the lowest (best) *FWHM* as determined from the ^{55}Fe radioisotope X-ray source measurements). The live time limit was chosen to be 120 s for all the ^{55}Fe X-ray spectra and 1000 s (1800 s) for the ^{109}Cd X-ray

and γ-ray spectra and the ^{241}Am X-ray and γ-ray spectra at 20 °C (temperature dependence spectra). An additional ^{109}Cd X-ray and γ-ray spectrum was accumulated with D1 at 20 °C with a longer live time (= 65 h) in order for the γ-ray photopeak at 88 keV to have sufficient counts for fitting. An additional (live time of 14 h) ^{241}Am X-ray and γ-ray spectrum was accumulated with D1 at 20 °C in order to provide an abundance of counts in the γ-ray peaks. The reported live times were chosen in order to provide sufficiently good counting statistics; the counts at the centroid channel number of the fitted photopeak were on the order of 10^3 counts.

The ^{55}Fe radioisotope X-ray source had an activity of 136 MBq and characteristic emission lines at Mn Kα (5.9 keV) and Mn Kβ (6.49 keV). It was placed 4 mm above the top of the array. Following accumulation of the ^{55}Fe X-ray spectra, the pixels were investigated for their spectroscopic performance at higher energies: The ^{109}Cd X-ray and γ-ray source had an activity of 390 MBq and characteristic emission lines at Ag $K\alpha_1$ (22.16 keV), $K\alpha_2$ (21.99 keV), Kβ (24.9 keV), Lα (2.98 keV) X-ray lines, and the 88 keV γ-ray line [29]. It was placed 6 mm above the top of the array. The ^{241}Am X-ray and γ-ray radioisotope source had an activity of 300 MBq and main characteristic emission lines at Np Lα (13.95 keV and 13.76 keV), Lβ (multiple lines ranging from 16.11 keV to 17.99 keV), and Lγ (multiple lines ranging from 20.78 keV to 21.49 keV) [30], and the γ-ray lines at 26.3 keV, 33.2 keV, 43.4 keV, and 59.54 keV [31]. It was placed 6 mm above the top of the array. All three sources were encapsulated in a stainless steel capsule, with a 0.25 mm thick Be window.

5.2. X-ray and γ-ray spectroscopy with all GaAs pixel detectors at 20 °C

An example ^{55}Fe X-ray spectrum obtained using the D1 at -50 V applied reverse bias and with a shaping time of 1 μs can be seen in **Fig. 7**. A main photopeak, the combination of the characteristic Mn Kα, at 5.9 keV, and Mn Kβ, at 6.49 keV, peaks of the radioisotope source [32], was detected. Gaussians were fitted to the detected photopeak of each spectrum, and the *FWHM* at 5.9 keV was deduced. The combined Mn Kα and Kβ peaks were fitted taking into account the relative emission ratio [32] and the relative quantum efficiency of the pixels at 5.9 keV and 6.49 keV. The energy calibration of the spectra was achieved using the position of the zero energy noise peak and the Mn Kα peak. The counts of the zero energy noise peak of the preamplifier were limited by setting the MCA low energy cut-off at ≈ 1 keV, however a small portion of the right hand side of the tail of the zero energy noise peak can still be seen (e.g. in **Fig. 7**). The counts at the left hand side of the photopeak outside of the fitted Gaussians, i.e. the low energy tailing of the ^{55}Fe X-ray photopeak, was attributed to charge created in the non-active layers of the pixel being partially collected. The amount of low energy tailing was quantified by the valley-to-peak ratio (*V*/*P*). The *V*/*P* was defined as the ratio between the number of counts within the low energy tailing (at the channel number corresponding to 3.5 keV) and the number of counts at the centroid channel number of the fitted Gaussian at 5.9 keV. *V*/*P* broadly improved as the *FWHM* at 5.9 keV improved (see discussion below); it ranged from 0.02 to 0.09, with an average value of 0.04 for all obtained ^{55}Fe X-ray spectra at 20 °C.

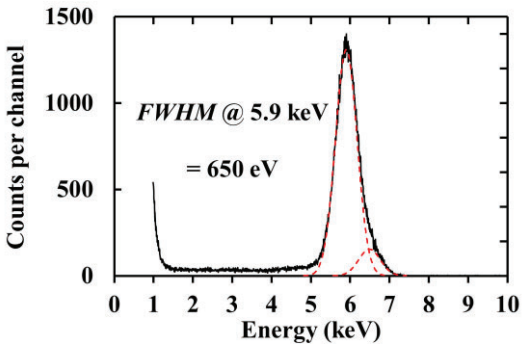

Figure 7. ^{55}Fe X-ray spectrum accumulated with the pixel D1 based spectrometer at a temperature of 20 °C. A reverse bias of -50 V was applied to the detector and a shaping time of 1 μs was used. The fitted Mn Kα and Kβ peaks (dashed lines) can also be seen.

The energy resolution (*FWHM* at 5.9 keV) achieved with each of the pixels was recorded. The best *FWHM* at 5.9 keV were: 650 eV (at 1 μs) with D1, 660 eV (at 1 μs) with D2, 640 eV (at 2 μs) with D3, and 670 eV (at 1 μs) with D4 (± 20 eV in each case). The mean was 650 eV ± 10 eV (rms error), corresponding to an equivalent noise charge (*ENC*) of 66 e^- rms ± 1 e^- rms. The uncertainty associated with the mean (± 10 eV, rms error) of those energy resolutions was smaller than the uncertainty of the *FWHM* associated with the Gaussian fitting to the photopeak, estimated to be ± 20 eV. Thus, it can be said that all four pixels had the same *FWHM* at 5.9 keV. The mean and rms error of the *FWHM* at 5.9 keV achieved among all four pixels, as a function of shaping time at 0 V, -5 V, and -50 V applied reverse bias, at 20 °C can be seen in **Fig. 8**. The variance of the energy resolution among the pixels at each applied reverse bias and shaping time was ≤ 20 eV. As can be seen from **Fig. 8**, the energy resolution improved when the reverse bias was applied. Discussion on the noise analysis of the spectrometer, and the effect of the reverse bias, shaping time, and temperature on the achieved energy resolution is presented in the following section.

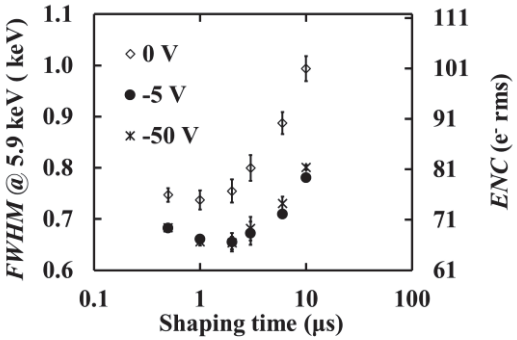

Figure 8. Mean and rms error of the *FWHM* at 5.9 keV achieved using all four pixels as a function of shaping time at three applied reverse biases (0 V, -5 V, and -50 V) at a temperature of 20 °C. The uncertainty of the *FWHM* associated with the Gaussian fitting to the photopeak was ± 20 eV.

The ^{109}Cd X-ray and γ-ray spectrum accumulated using D1 at 20 °C (at the optimum reverse bias, -50 V, and available shaping time, 1 μs), can be seen in **Fig. 9**. The characteristic Ag Lα, $K\alpha_1$ and $K\alpha_2$ (combined, not being individually resolved), and Kβ X-ray peaks, along with the γ-ray peak, can be seen in the spectrum. The Ag Kα and Kβ X-ray photons, and the 88 keV γ-ray photons were able to fluoresce the Ga and As atoms in the detectors, thus giving rise to the Ga and As fluorescence peaks visible in the spectra at energies between 9.225 keV (Ga $K\alpha_2$) and 11.726 keV (As $K\beta_1$), that can be seen in **Fig. 9**. Additionally, Ga and As escape peaks associated with Ag K shell photons and the γ-ray line were also visible. Fluorescence peaks of the stainless steel ^{109}Cd radioisotope source capsule are also apparent at 5.4 keV (Cr K_α) and 6.4 keV (Fe Kα). Five peaks at ≈ 44 keV, 47 keV, 67 keV, 69 keV, and 73 keV were evidence of pulse pile-up [33] from different combinations of Ag Kα and Kβ X-ray photons.

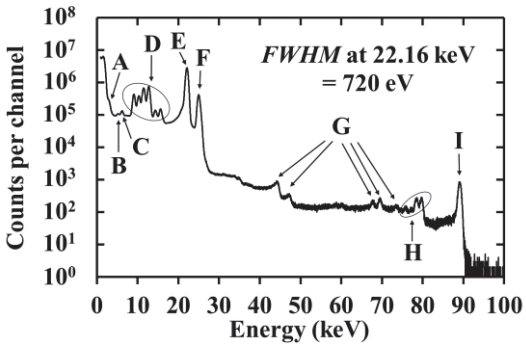

Figure 9. ^{109}Cd X-ray and γ-ray spectrum accumulated with the pixel D1 based spectrometer at 20 °C (-50 V reverse bias and 1 μs shaping time). The major peaks identified are: (A) Ag La peak; (B) Cr Kα peak; (C) Fe Kα peak; (D) Ga and As fluorescence and escape peaks; (E) combined Ag $K\alpha_1$ and $K\alpha_2$ peak; (F) Ag Kβ peak; (G) pulse pile up peaks from combinations of Ag Kα and Kβ X-ray photons; (H) Ga and As escape peaks from 88 keV γ-ray photons; (I) 88 keV γ-ray peak. The counts (≈ 1000) beyond the 88 keV γ-ray peak corresponded to full or incomplete collection of charge resulted from pile up.

The combined Ag Kα and Kβ lines were fitted taking into account the relative emission ratio [29] and the relative quantum efficiency of the pixels at 21.99 keV and 22.16 keV. The energy calibration of the spectra was achieved using the position of the zero energy noise peak and the position of the Ag Kα peak. The counts of the zero energy noise peak of the preamplifier were limited by setting the MCA low energy cut-off to ≈ 1 keV, however a small portion of the right hand side of the tail of the zero energy noise peak can still be seen (e.g. in **Fig. 10**). The *FWHM* at 22.16 keV was 710 eV with D1, 740 eV with D2, 750 eV with D3, and 790 eV with D4 (± 20 eV in each case), with a mean of 750 eV ± 30 eV (rms error), corresponding to an equivalent noise charge (*ENC*) of 75 e^- rms ± 3 e^- rms. The uncertainty associated with the mean (± 30 eV, rms error) was greater than the uncertainty associated with the direct measurement of each *FWHM* at 22.16 keV (which was ± 20 eV), therefore on this basis it cannot be said that all four pixels had the same *FWHM* at 22.16 keV. However, the mean *FWHM* at 22.16 keV of pixels D1 – D3, i.e. excluding D4, was 730 eV ± 20 eV, thus in these strict terms it can be said that those three pixels had the same *FWHM* at 22.16 keV. Nevertheless, given the low numbers of pixels considered, the statistical significance of the difference in uncertainty associated with the mean and directly measured *FWHM* of the four pixels was not major; it is noted here simply for completeness. The 88 keV γ-ray photopeak of the long duration accumulation was also fitted with an appropriate Gaussian (**Fig. 9**); the *FWHM* at 88 keV was 820 eV ± 20 eV.

The ^{241}Am X-ray and γ-ray spectrum accumulated using D1 at 20 °C (and the optimum reverse bias, -50 V, and optimum available shaping time, 1 μs), can be seen in **Fig. 10**. The characteristic Np Lα, Lβ, and Lγ X-ray peaks and the γ-ray peaks at 26.3 keV, 33.2 keV, 43.4 keV, and 59.54 keV are well apparent in the spectrum. The X-ray and γ-ray photons emitted from the source were able to fluoresce the Ga and As atoms in the detectors similarly as was seen with the ^{109}Cd radioisotope X-ray/γ-ray source. Ga and As escape peaks were formed from the Np L X-ray lines and the γ-ray lines. Fluorescence of the stainless steel ^{241}Am source capsule at 6.4 keV (Fe Kα) and 5.4 keV (Cr Kα) was also visible.

The 59.54 keV γ-ray peak was fitted with an appropriate Gaussian; energy calibration of each spectrum was achieved using the position of the zero energy noise peak and the position of the 59.54 keV γ-ray peak. Again, the MCA low energy cut-off was set at ≈ 1 keV to limit the counts of the zero energy noise peak. The *FWHM* at 59.54 keV was 720 eV with D1 and D2, 730 eV with D3, and 740 eV with D4 (± 20 eV in each case). The mean *FWHM* was 730 eV ± 10 eV, corresponding to an equivalent noise charge (*ENC*) of 74 e^- rms ± 1 e^- rms. The uncertainty associated with the mean (±

10 eV, rms error) energy resolution (*FWHM* at 59.54 keV) among the pixels was within the uncertainty of the *FWHM* associated with the Gaussian fitting to the photopeak, estimated to be ± 20 eV. Thus the pixels all had the same energy resolution.

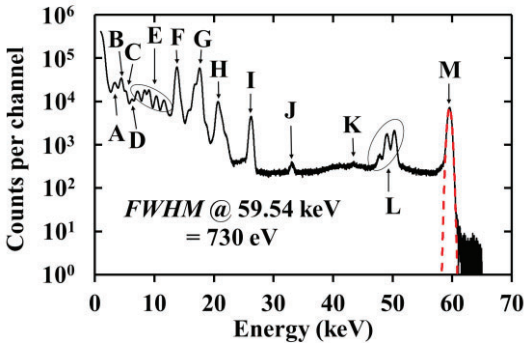

Figure 10. ^{241}Am X-ray and γ-ray spectrum accumulated with the pixel D1 based spectrometer at 20 °C (-50 V reverse bias and 1 μs shaping time). The fitted 59.54 keV γ-ray peak (red dashed lines) can also be seen. The major peaks identified are: (A) Ga Kβ escape peak from the Np Lα X-ray photons; (B) Ga Ka escape peak from the Np Lα X-ray photons; (C) Cr Kα peak; (D) Fe Kα peak; (E) Ga and As fluorescence and escape peaks; (F) Np Lα peak; (G) Np Lβ peak; (H) Np Lγ peak; (I) 26.3 keV γ-ray peak; (J) 33.2 keV γ-ray peak; (K) 43.4 keV γ-ray peak; (L) Ga and As escape peaks from 59.54 keV γ-ray photons; (M) 59.54 keV γ-ray peak. The counts (≈ 1200) beyond the 59.54 keV γ-ray peak corresponded to full or incomplete collection of charge resulted from pile up.

A summary of the optimum operating conditions (for the best energy resolution) and the achieved energy resolution at different energies with the reported X-ray and γ-ray spectrometer using all four GaAs pixels (D1 to D4) can be seen in **Table 3**.

Table 3. The *FWHM* at different energies, along with the optimum operating conditions (for best energy resolution) of the reported X-ray and γ-ray spectrometer operating at 20 °C, using all four GaAs pixels.

Pixel	Optimum bias (V)	Optimum shaping time (μs)	*FWHM* (eV) ± 20 eV @		
			5.9 keV	22.16 keV	59.54 keV
D1	-50	1	650	710	720
D2	-50	1	660	740	720
D3	-50	2	640	750	730
D4	-50	1	670	790	740

The results presented in **Table 3** are important: the energy resolution of the each pixel spectrometer agreed within the uncertainties associated with the Gaussian fitting of the photopeaks (excluding that of D4 at 22.16 keV). The uncertainty associated with the mean energy resolution achieved with all the pixel spectrometers (± 30 eV, rms error) was ≤ 4 % of each measured *FWHM* at all three energies. Comparing to the previous report on a room temperature GaAs pixel array, four of the pixels from the 32 × 32 pixel array [23] were characterised; their energy resolutions were the same within 20 % of each other (cf. 4 % for the detectors reported presently). However, the energy resolutions reported by Erd et al. [23] (300 eV *FWHM* at 5.9 keV and 650 eV *FWHM* at 59.54 keV, at room temperature) were better than that measured for the currently reported pixels (650 eV ± 10 eV *FWHM* at 5.9 keV and 730 eV ± 10 eV *FWHM* at 59.54 keV, at room temperature). This was, in part, due to a thicker epitaxial i layer (325 μm [23] cf. 10 μm for the pixels reported here), which in turn improved (increased) the quantum detection efficiency relative to that reported here.

5.3. Temperature dependence X-ray and γ-ray spectroscopy with pixel D1

The accumulated ^{55}Fe X-spectra with the best energy resolution (*FWHM* at 5.9 keV) at 100 °C (-5 V reverse bias and 0.5 μs shaping time) and 20 °C (-50 V reverse bias and 1 μs shaping time) can be seen in **Fig. 11**. The spectra were energy calibrated and analysed as previously. The *V*/*P* ratio improved (decreased) with decreasing temperature; the best recorded *V*/*P* ratios improved from 0.10 at 100 °C (-5 V reverse bias and 0.5 μs shaping time) to 0.02 at 20 °C (-50 V reverse bias and 2 μs shaping time). The *FWHM* at 5.9 keV was measured for all accumulated spectra; it decreased from 1.61 keV ± 0.04 keV at 100 °C (-5 V reverse bias and 0.5 μs shaping time) to 0.65 keV ± 0.02 keV at 20 °C (-50 V reverse bias and 1 μs shaping time).

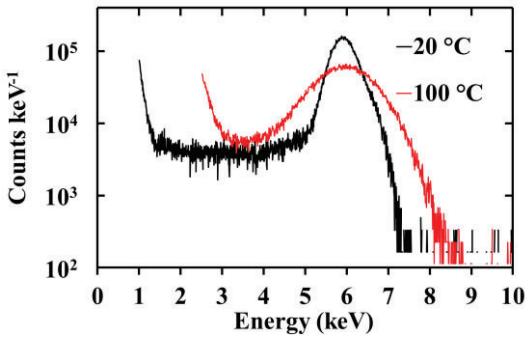

Figure 11. Comparison between the ^{55}Fe X-ray spectra accumulated with the pixel D1 based spectrometer at 100 °C (-5 V reverse bias and 0.5 μs shaping time; *FWHM* at 5.9 keV = 1.61 keV ± 0.04 keV; red line) and at 20 °C (-50 V reverse bias and 1 μs shaping time; *FWHM* at 5.9 keV = 0.65 keV ± 0.02 keV; black line).

The *FWHM* at 5.9 keV as a function of shaping time, at 0 V, -5 V, and -50 V applied reverse bias, at all investigated temperatures can be seen in **Fig. 12**. The range of the *y*-axes of all parts of **Fig. 12** are identical to emphasize the improvement of the energy resolution with every 20 °C decrease. The combined Mn Kα and Kβ photopeak at 100 °C could not be resolved from the zero energy noise peak at long shaping times (i.e. 10 µs for -5 V applied reverse bias and ≥ 2 µs for -50 V reverse bias). This is discussed in the noise analysis of the spectroscopic system which follows. Of the available shaping times and applied reverse biases used, the best *FWHM* at 5.9 keV was achieved with the pixel D1 based spectrometer at 0.5 µs and -5 V (and 0 V) at 100 °C, 0.5 µs and -5 V at 80 °C, 1 µs and -5 V at 60 °C, 1 µs and -5 V (and -50 V) at 40 °C, 1 µs and -5 V (and -50 V) at 20 °C. **Figure 12** suggests that an applied reverse bias between -5 V and -50 V may have resulted in an improved energy resolution at 80 °C and 60 °C.

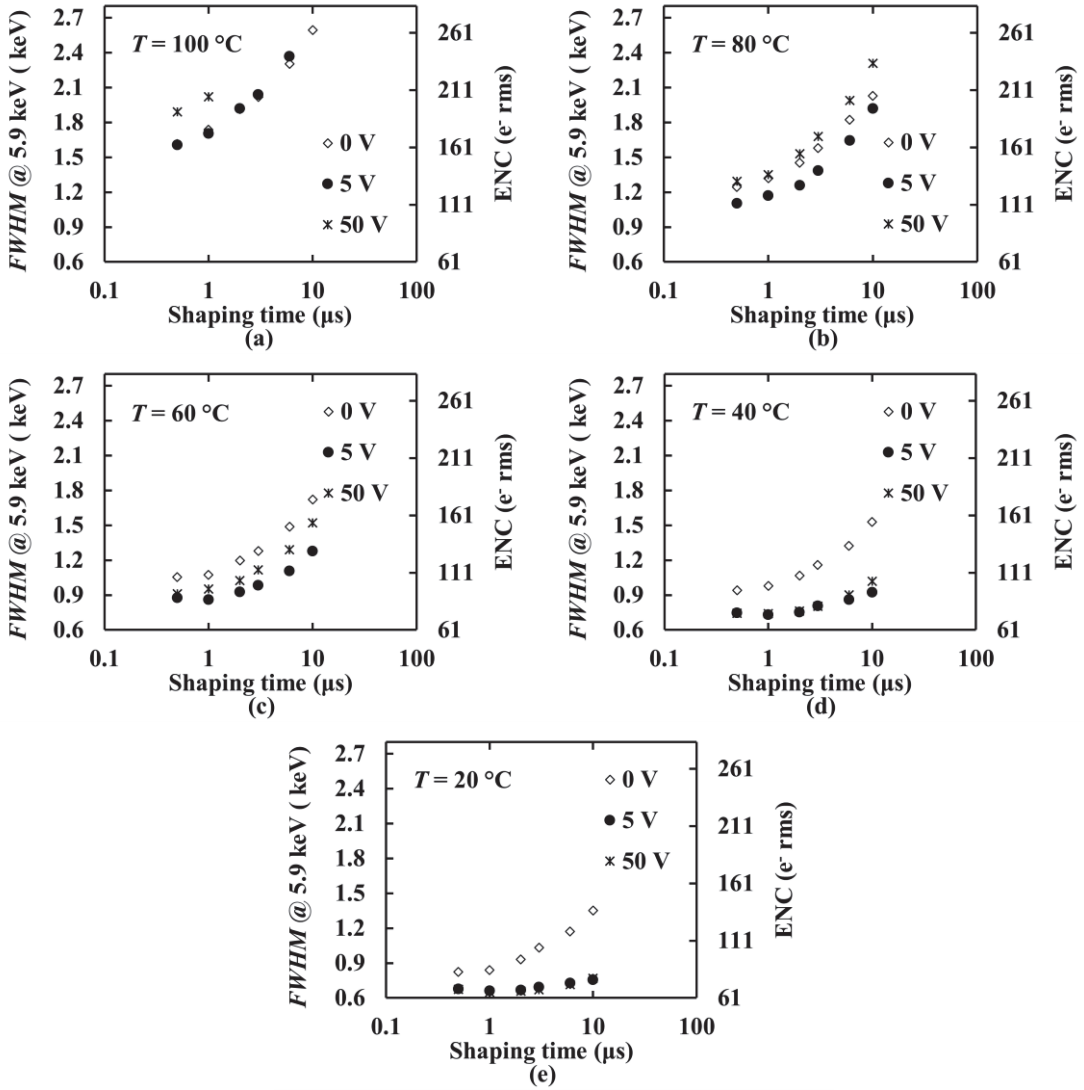

Figure 12. *FWHM* at 5.9 keV as a function of shaping time at three applied reverse biases (0 V, -5 V, and -50 V) with the pixel D1 and the preamplifier operated at: (a) 100 °C; (b) 80 °C; (c) 60 °C; (d) 40 °C; and (e) 20 °C.

Three independent terms, the Fano noise, the incomplete charge collection noise, and the electronic noise, define the energy resolution of a non-avalanche photodiode based photon counting X-ray spectrometer [34]. The Fano noise arises due to the statistical nature of the ionisation process [35] and is a function of photon energy. The incomplete charge collection noise results from crystal

imperfections leading to charge carrier trapping and recombination; it is also photon energy dependent [19]. The electronic noise, which is photon energy independent, consists of the white series noise (including the induced gate current noise), the white parallel noise, 1/*f* noise, and the dielectric noise [34].

The white series noise is inversely proportional to the shaping time; it depends on the total capacitance (detector capacitance, input JFET capacitance, feedback capacitance, and stray capacitance). The white parallel noise is proportional to the shaping time; it depends on the total leakage current (leakage current of the detector and the input JFET). The best energy resolution (lowest *FWHM* at a given energy) is achieved at a shaping time (the optimum shaping time) where the quadratic summation of the white series and white parallel noise is minimised. The 1/*f* and dielectric noises are shaping time invariant.

The relatively broad *FWHM* at 5.9 keV at high temperatures (100 °C) and long shaping times, which prohibited the photopeak from being resolved from the zero energy noise peak, was attributed to the high total leakage current, when the detector was reverse biased. The improvement of the energy resolution with decreased temperature was mainly attributed to the decreased white parallel noise and dielectric noise, with decreasing temperature.

Fitting the experimental values of the *FWHM* at 5.9 keV as a function of shaping time, through a multidimensional least squares estimation method, allowed the determination of the shaping time inversely proportional (white series), shaping time directly proportional (white parallel), and shaping time invariant (quadratic sum of incomplete charge collection, Fano, 1/*f*, and dielectric) noise contributions to be determined [36]. The multidimensional nonlinear fitting of the *FWHM* at 5.9 keV as a function of shaping time at 100 °C (-5 V reverse bias) and 20 °C (-50 V reverse bias), can be seen in **Fig. 13**.

The Fano noise and the 1/*f* noise were calculated and subtracted in quadrature from the shaping time invariant contribution, to result in the combined contribution of the incomplete charge collection (if present) and dielectric noise. The Fano noise was calculated at 5.9 keV, assuming a Fano factor of 0.12 [18] and a temperature, *T* (in Kelvin), dependent electron hole pair creation energy, $\omega = 4.55 - 0.00122T$ [15]. The 1/*f* noise was calculated based on Ref. [34]; its contribution was found to be minimal (< 5 e^- rms) at both temperatures, in comparison to the rest of the noise contributions.

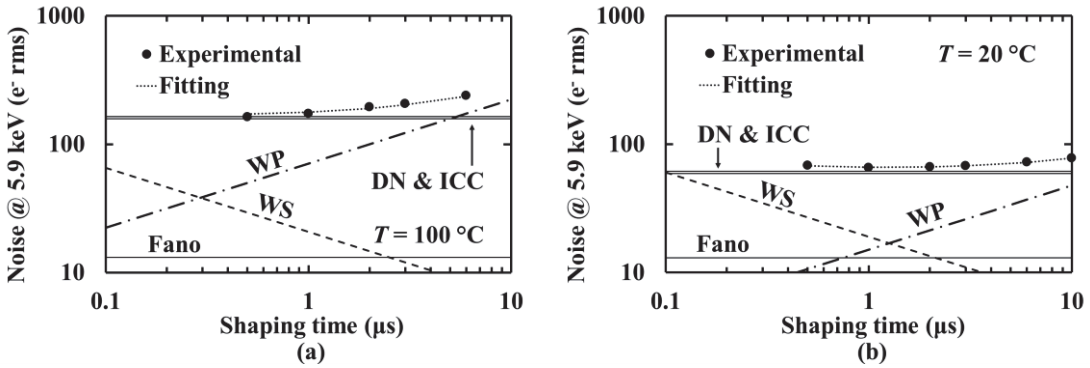

Figure 13. Equivalent noise charge at 5.9 keV for the pixel D1 based spectrometer as a function of shaping time at: (a) 100 °C (-5 V reverse bias) and (b) 20 °C (-50 V reverse bias). The multidimensional least squares fitting of the experimental points (dotted line), the white parallel noise (WP, dashed dotted line), the white series noise (WS, dashed line), the Fano noise (solid line), and the quadratic sum of the dielectric and incomplete charge collection noise (DN & ICC, double solid line) are also shown.

The optimum available shaping time was found to be 0.5 μs at the highest investigated temperature, 100 °C, and -5 V reverse bias. A better energy resolution could have been achieved having a shorter shaping time; **Fig. 13** suggests that 0.3 μs shaping time was the optimum shaping time, but this was not available on the 572A shaping amplifier used. The dominant source of noise at 100 °C, when D1 was reverse biased at -5 V, was the quadratic sum of dielectric noise and incomplete charge collection noise for a shaping time < 6 μs and the white parallel noise for a shaping time ≥ 6 μs. However, the quadratic sum of dielectric noise and incomplete charge collection noise was the dominant source of noise at all investigated shaping times at an operating temperature of 20 °C and a detector bias of -50 V. The quadratic sum of dielectric noise and incomplete charge collection noise was calculated to decrease from 161 e^- rms at 100 °C (-5 V applied reverse bias) to 60 e^- rms at 20 °C (-50 V applied reverse bias). The dielectric noise of a photodiode based X-ray and γ-ray spectrometer results from all the lossy dielectrics at the input of the preamplifier. These include the feedback capacitance, the input JFET dielectrics, passivation, and packaging, and the detector and its packaging [36-38].

The total leakage current of the spectrometer, including both the contribution of the pixel (D1) leakage current and the input JFET leakage current, was estimated from the τ dependent contribution of the multidimensional least squares fitting of the measured *FWHM* at 5.9 keV as a function of shaping time (**Fig. 13**). It was found to decrease from 433 pA at 100 °C (-5 V reverse bias) to 20 pA at 20 °C (-50 V reverse bias). Similarly, the total capacitance of the spectrometer, including the detector, input JFET, feedback, and stray capacitances, was estimated from the inversely τ dependent contribution of the multidimensional least squares fitting of the measured *FWHM* at 5.9 keV as a function of shaping time (**Fig. 13**). It was found to decrease from of 2.6 pF at 100 °C (-5 V reverse bias) to 2.3 pF at 20 °C (-50 V reverse bias).

The effect of the temperature on the energy resolution (*FWHM* at 5.9 keV) of the spectrometer can be seen in **Fig. 14**. The *FWHM* at 5.9 keV as a function of temperature achieved using a previously reported circular mesa GaAs p^+-i-n^+ diode (200 μm diameter) [25] made from material of the same epiwafer as the array reported here, is also shown in **Fig. 14** for comparison purposes. The charge-sensitive preamplifier electronics of the two systems were similar, but not identical. The best (lowest) *FWHM* at 5.9 keV at 100 °C was 2.00 keV with the previously reported photodiode detector [25] and 1.61 keV ± 0.04 keV with the new detector reported here. The difference in energy resolution between the two spectrometers reduced as the temperature was decreased: the best *FWHM* at 5.9 keV at 20 °C was 0.69 keV with the previously reported spectrometer and 0.65 keV ± 0.02 keV with D1. The better energy resolution (mainly at high temperatures) of the new spectrometer with the square pixels, was attributed to the lower leakage current at high temperatures [25] as well as to possible smaller leakage current contribution of the input JFET to the total noise of the currently reported spectrometer compared to the one reported in Ref. [25]. It should be noted that the currently reported square pixel geometry is more beneficial for a detector array relative to a circular pixel geometry, by virtue of an improved (increased) detector fill factor (ratio between the area covered by the pixels to the total area of the detector array). For example a fill factor of 81 % and 63 % was calculated for a 2 × 2 pixel array having 200 μm × 200 μm square pixels and 200 μm diameter circular pixels, respectively.

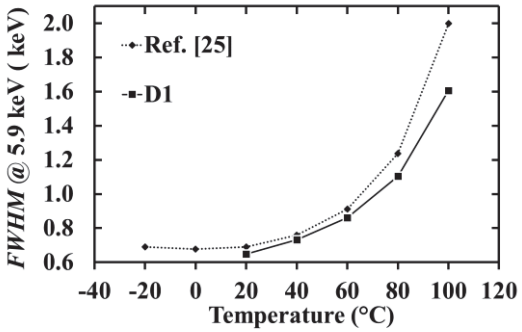

Figure 14. Comparison of the best *FWHM* at 5.9 keV as a function of temperature obtained using a circular mesa GaAs p^+-i-n^+ diode (diamonds) [25] and the pixel D1 based spectrometer reported here (circles). The preamplifier electronics were similar but not identical.

The accumulated ^{109}Cd X-ray and γ-ray spectra at 100 °C and 20 °C, can be seen in **Fig. 15**. The broadening of the energy resolution at 100 °C compared to that at 20 °C is apparent; the *FWHM* at 22.16 keV improved from 1.63 keV ± 0.06 keV at 100 °C (-5 V reverse bias and 0.5 μs shaping time) to 0.69 keV ± 0.02 keV at 20 °C (-50 V reverse bias and 1 μs shaping time). The Ag Kα and Kβ photopeaks were less well separated at 100 °C compared to 20 °C. In addition, the MCA low energy cut-off was set to higher energy at 100 °C (2.5 keV) compared to that at 20 °C (1 keV), to limit the counts of the zero energy noise peak.

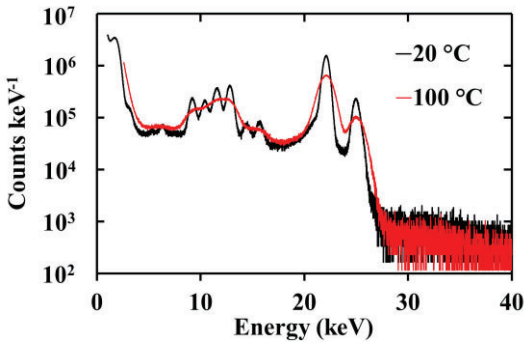

Figure 15. Comparison between the ^{109}Cd X-ray and γ-ray spectra accumulated with the pixel D1 based spectrometer at 100 °C (-5 V reverse bias and 0.5 μs shaping time, *FWHM* at 22.16 keV = 1.63 keV ± 0.06 keV) and at 20 °C (-50 V reverse bias and 1 μs shaping time, *FWHM* at 22.16 keV = 0.69 keV ± 0.02 keV).

The accumulated ^{241}Am X-ray and γ-ray spectra at 100 °C and 20 °C, can be seen in **Fig. 16**. The *FWHM* at 59.54 keV improved from 1.65 keV ± 0.08 keV at 100 °C (-5 V reverse bias and 0.5 μs shaping time) to 0.73 keV ± 0.02 keV at 20 °C (-50 V reverse bias and 1 μs shaping time). A summary of the best energy resolutions, *FWHM* at 5.9 keV, 22.16 keV, and 59.54 keV, of the reported spectrometer achieved at different temperatures can be seen in **Table 4**. The total noise excluding the Fano noise, i.e. the quadratic sum of the electronic and incomplete charge collection noise (if present), is also reported in **Table 4**. These results allowed investigation of the presence of incomplete charge collection noise.

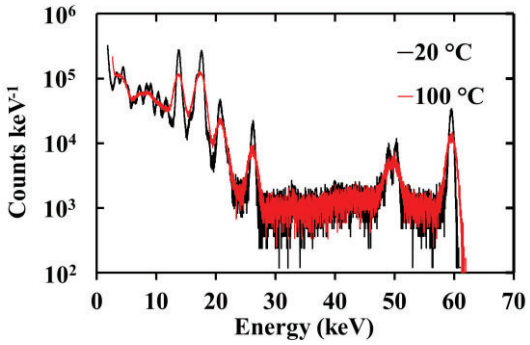

Figure 16. Comparison between the ^{241}Am spectra accumulated with the pixel D1 based spectrometer at 100 °C (-5 V reverse bias and 0.5 µs shaping time, *FWHM* at 59.54 keV = 1.65 keV ± 0.08 keV) and at 20 °C (-50 V reverse bias and 1 µs shaping time, *FWHM* at 59.54 keV = 0.73 keV ± 0.02 keV).

The electronic noise is energy independent whereas the incomplete charge collection noise depends on the photon energy. Hence, the quadratic sum of the electronic and incomplete charge collection noise (i.e. total noise contributions excluding the Fano noise) as a function of photon energy allowed investigation of the presence (or absence) of incomplete charge collection noise. As can be seen from **Table 4**, subtracting in quadrature the Fano noise from the total noise resulted in an energy invariant remainder. The mean value and the rms error of the quadratic sum of the electronic and incomplete charge collection noise among the three different energies was calculated at each temperature and was found to be 1.60 keV ± 0.01 keV at 100 °C, 1.10 keV ± 0.01 keV at 80 °C, 0.87 keV ± 0.02 keV at 60 °C, 0.73 keV ± 0.02 keV at 40 °C, and 0.63 keV ± 0.02 keV at 20 °C. Thus, it can be concluded that the pixel did not suffer from incomplete charge collection within the investigated temperature and energy ranges.

Table 4. A summary of the *FWHM* at three energies (5.9 keV, 22.16 keV, and 59.54 keV) of the pixel D1 based spectrometer as a function of temperature. The total noise, when the Fano noise was excluded, i.e. the quadratic sum of the electronic and incomplete charge collection noise (if present), is also shown.

T **(° C)**	***FWHM*** **(keV) @**			***FWHM*** **(keV) excl. Fano noise @**		
	5.9 keV	**22.16 keV**	**59.54 keV**	**5.9 keV**	**22.16 keV**	**59.54 keV**
100	1.61 ± 0.04	1.63 ± 0.06	1.65 ± 0.08	1.60 ± 0.04	1.61 ± 0.06	1.60 ± 0.08
80	1.11 ± 0.03	1.12 ± 0.03	1.17 ± 0.04	1.10 ± 0.03	1.09 ± 0.03	1.10 ± 0.04
60	0.86 ± 0.02	0.93 ± 0.02	0.96 ± 0.03	0.85 ± 0.02	0.90 ± 0.02	0.87 ± 0.03
40	0.73 ± 0.02	0.79 ± 0.02	0.81 ± 0.02	0.72 ± 0.02	0.75 ± 0.02	0.71 ± 0.02
20	0.65 ± 0.02	0.69 ± 0.02	0.73 ± 0.02	0.64 ± 0.02	0.64 ± 0.02	0.60 ± 0.02

6. Conclusions

A GaAs 2 × 2 pixel monolithic X-ray detector array was investigated for its photon counting X-ray and γ-ray spectroscopic performance at photon energies up to 88 keV, operating uncooled within the temperature range 100 °C to 20 °C. Each pixel was a square mesa p^+-i-n^+ photodiode with an area of 200 µm × 200 µm and a 10 µm i layer.

Comparable and low leakage currents were measured for all four pixels at 20 °C; a mean leakage current of 3.9 pA ± 0.5 pA (rms error) at -50 V applied reverse bias (50 kV/cm electric field strength) was measured. The leakage current of D1, a representative pixel operated at -50 V applied reverse bias, decreased from 1.281 nA ± 0.006 nA at 100 °C to 4.1 pA ± 0.4 pA at 20 °C; its leakage current

density was lower compared to previously reported high quality GaAs X-ray photodiode detectors. The i layer of D1 was found to be almost fully depleted at -5 V; it was 97 % depleted at 100 °C and 98 % depleted at 20 °C. This was achieved due to the relatively low effective carrier concentration in its intrinsic layer.

Each pixel was used for photon counting X-ray and γ-ray spectroscopy at 20 °C; their performance was characterized using ^{55}Fe X-ray, ^{109}Cd X-ray and γ-ray, and ^{241}Am X-ray and γ-ray radioisotope sources. The mean *FWHM* measured were: 650 eV ± 10 eV at 5.9 keV; 750 eV ± 30 eV at 22.16 keV, and 730 eV ± 10 eV at 59.54 keV. Analysis of ^{55}Fe X-ray spectra accumulated using the D1 based spectrometer within the temperature range 100 °C to 20 °C, as a function of shaping time and applied reverse bias, allowed the separation of the different noise contributions and the identification of the dominant source of noise in the spectrometer. The dominant source of noise at 100 °C was the white parallel noise (due to the combined leakage current of the pixel and input JFET) at long shaping times (≥ 6 μs), and the dielectric noise at short shaping times (< 6 μs), when a -5 V reverse bias was applied. The dielectric noise was found to be the dominant source of noise at 20 °C for all available shaping times when a -50 V reverse bias was applied to the detector. The electronic noise contribution decreased from 1.60 keV ± 0.01 keV at 100 °C to 0.63 keV ± 0.02 keV at 20 °C. It was found that pixel D1 (and presumably the other pixels) did not suffer from incomplete charge collection within the temperature and energy ranges investigated.

The presently reported small GaAs array yielded the best X-ray and γ-ray energy resolution yet reported for GaAs detectors at high temperatures (> 20 °C). The *FWHM* achieved when the array and preamplifier was operated at 100 °C was 1.61 keV ± 0.04 keV at 5.9 keV, 1.63 keV ± 0.06 keV at 22.16 keV, and 1.65 keV ± 0.08 keV at 59.54 keV. The results demonstrate that small mesa pixel X-ray and γ-ray photodiode arrays can now be produced and that they are suitable for X-ray and γ-ray photon counting spectroscopy, even at high temperatures (operating uncooled at temperatures ≤ 100 °C). In reaching this milestone, the agenda is now set and a path is clear towards larger monolithic GaAs mesa pixel photodiodes for X-ray and γ-ray photon counting spectroscopic imaging. In future work, arrays with larger numbers of pixels shall be reported, as shall improvements to the preamplifier electronics including adaptions for operation at temperatures > 100 °C. Application-Specific Integrated Circuits (ASICs) may be considered for the read out electronics of arrays with larger numbers of pixels, such as that reported by Bertuccio & Caccia [39], where noise levels of a few e- rms were achieved. Alternatively hybrid arrays, in which the pixels and the input preamplifiers are mounted directly on the same substrate to minimise the dielectric noise and the stray capacitance, similar to the GaAs 4 × 4 pixel detector array reported by Owens et al. [40], can also be utilised in future larger arrays detectors. The size and number of pixels of future larger arrays will be dictated in part by the uniformity achieved across pixels which is both a consequence of the epitaxial wafer uniformity and of perfection of the fabrication process; an increase of pixel size and number is expected over time, with the ultimate size of a monolithic array being limited by the wafer diameter itself.

DATA AVAILABILITY

Data underlying this work are subject to commercial confidentiality. The Authors regret that they cannot grant public requests for further access to any data produced during the study, however the key findings are fully included within the article.

ACKNOWLEDGEMENTS

This work was in part supported by the Science and Technology Facilities Council, UK, via grants ST/T000910/1 and ST/P001815/1 (University of Sussex, A.M.B., PI). A.M.B. acknowledges funding from the Leverhulme Trust, United Kingdom, in the form of a 2016 Philip Leverhulme Prize. The authors are grateful to B. Harrison, R. J. Airey, and S. Kumar at the EPSRC National Epitaxy Facility

for material growth and device fabrication and to M.D.C. Whitaker, at the University of Sussex, for LabVIEW script development for data acquisition.

REFERENCES

[1] M.C. Weisskopf, B. Brinkman, C. Canizares, G. Garmire, S. Murray, L.P. Van Speybroeck, An Overview of the Performance and Scientific Results from the Chandra X-Ray Observatory, Publications of the Astronomical Society of the Pacific, 114 (2002) 1-24.

[2] L. Strüder et al., The European Photon Imaging Camera on XMM-Newton: The pn-CCD Camera, Astronomy and Astrophysics, 365 (2001) L18-L26.

[3] D.N. Burrows, J.E. Hill, J.A. Nousek, J.A. Kennea, A. Wells, J.P. Osborne, A.F. Abbey, A. Beardmore, K. Mukerjee, A.D.T. Short, G. Chincarini, S. Campana, O. Citterio, A. Moretti, C. Pagani, G. Tagliaferri, P. Giommi, M. Capalbi, F. Tamburelli, L. Angelini, G. Cusumano, H.W. Bräuninger, W. Burkert, G.D. Hartner, The SWIFT X-ray Telescope, Space Science Reviews, 120 (2005) 165-195.

[4] K. Koyama et al., X-Ray Imaging Spectrometer (XIS) on Board Suzaku, Publications of the Astronomical Society of Japan, 59 (2007) S23-S33.

[5] A.F. Abbey, P.J. Bennie, M.J.L. Turner, B. Altieri, S. Rives, Cooling out the Radiation Damage on the XMM-Newton EPIC MOS CCDs, Nuclear Instruments and Methods in Physics Research A, 513 (2003) 136-142.

[6] J. Benkhoff, J.V. Casterena, H. Hayakawa, M. Fujimoto, H. Laakso, M. Novaraa, P. Ferri, H.R. Middleton, R. Ziethea, BepiColombo—Comprehensive exploration of Mercury: Mission overview and science goals, Planetary and Space Science, 58 (2010) 2-20.

[7] G.W. Fraser, J.D. Carpenter, D.A. Rothery, J.F. Pearson, A. Martindale, J. Huovelin, J. Treis, M. Anand, M. Anttila, M. Ashcroft, J. Benkoff, P. Bland, A. Bowyer, A. Bradley, J. Bridges, C. Brown, C. Bulloch, E.J. Bunce, U. Christensen, M. Evans, R. Fairbend, M. Feasey, F. Giannini, S. Hermann, M. Hesse, M. Hilchenbach, T. Jorden, K. Joy, M. Kaipiainen, I. Kitchingman, P. Lechner, G. Lutz, A. Malkki, K. Muinonen, J.Naranen, P. Portin, M. Prydderch, J. San Juan, E. Sclater, E. Schyns, T.J. Stevenson, L. Struder, M. Syrjasuo, D. Talboys, P. Thomas, C. Whitford, S. Whitehead, The Mercury Imaging X-ray Spectrometer (MIXS) on Bepicolombo, Planetary and Space Science, 58 (2010) 79-95.

[8] J.H. Hubbell, S.M. Seltzer, Tables of X-Ray Mass Attenuation Coefficients and Mass Energy-Absorption Coefficients (Version 1.4), National Institute of Standards and Technology, Gaithersburg, 2004.

[9] K.P. Singh et al., ASTROSAT mission, SPIE proceedings, Space Telescopes and Instrumentation: Ultraviolet to Gamma Ray, 9144 (2014) 91441S.

[10] S.D. Barthelmy, L.M. Barbier, J.R. Cummings, E.E. Fenimore, N. Gehrels, D. Hullinger, H.A. Krimm, C.B. Markwardt, D.M. Palmer, A. Parsons, G. Sato, M. Suzuki, T. Takahashi, M. Tashiro, J. Tueller, The Burst Alert Telescope (BAT) on the SWIFT Midex Mission, Space Science Reviews, 120 (2005) 143-164.

[11] M. Sammartini, M. Gandola, F. Mele, B. Garavelli, D. Macera, P. Pozzi, G. Bertuccio, A CdTe pixel detector–CMOS preamplifier for room temperature high sensitivity and energy resolution X and γ ray spectroscopic imaging, Nuclear Instruments and Methods in Physics Research A, 910 (2018) 168-173.

[12] A.G. Kozorezov, J.K. Wigmore, A. Owens, R. den Hartog, A. Peacock, H.A. Al-Jawhari, Resolution Degradation of Semiconductor Detectors due to Carrier Trapping, Nuclear Instruments and Methods in Physics Research A, 546 (2005) 209-212.

[13] C.T.C. Hansson, A. Owens, J. van den Biezen, X-ray, γ-ray and Neutron Detector Development for Future Space Instrumentation, Acta Astronautica, 93 (2014) 121-128.

[14] A. Owens, M. Bavdaz, A. Peacock, A. Poelaert, H. Andersson, S. Nenonen, H. Sipila, L. Tröger, G. Bertuccio, High Resolution X-Ray Spectroscopy Using GaAs Arrays, Journal of Applied Physics, 90 (2001) 5376-5381.

[15] G. Bertuccio, D. Maiocchi, Electron-Hole Pair Generation Energy in Gallium Arsenide by x and γ Photons, Journal of Applied Physics, 92 (2002) 1248-1255.
[16] W. Bludau, A. Onton, W. Heinke, Temperature Dependence of the Band Gap of Silicon, Journal of Applied Physics, 45 (1974) 1846-1848.
[17] S. Del Sordo, L. Abbene, E. Caroli, A.M. Mancini, A. Zappettini, P. Ubertini, Progress in the Development of CdTe and CdZnTe Semiconductor Detectors for Astrophysical and Medical Applications, Sensors, 9 (2009) 3491-3526.
[18] G. Bertuccio, A. Pullia, J. Lauter, A. Forster, H. Luth, Pixel X-ray Detectors in Epitaxial Gallium Arsenide with High-Energy Resolution Capabilities (Fano Factor Experimental Determination), IEEE Transactions on Nuclear Science, 44 (1997) 1-5.
[19] A. Owens, A. Peacock, Compound semiconductor radiation detectors, Nuclear Instruments and Methods in Physics Research A, 531 (2004) 18-37.
[20] B.G. Lowe, R.A. Sareen, A measurement of the electron–hole pair creation energy and the Fano factor in silicon for 5.9 keV X-rays and their temperature dependence in the range 80–270 K, Nuclear Instruments and Methods in Physics Research A, 576 (2007) 367-370.
[21] J. Huovelin, R. Vainio, H. Andersson, E. Valtonen, L. Alha, A.Malkki, M. Grande, G.W. Fraser, M. Kato, H. Koskinen, K. Muinonen, J. Naranen, W. Schmidt, M. Syrjasuo, M. Anttila, T. Vihavainen, E. Kiuru, M. Roos, J. Peltonen, J. Lehti, M. Talvioja, P. Portin, M. Prydderch, Solar Intensity X-ray and particle Spectrometer (SIXS), Planetary and Space Science, 58 (2010) 96-107.
[22] V. Bhalerao, D. Bhattacharya, A. Vibhute, P. Pawar, A. R. Rao, M. K. Hingar, Rakesh Khanna, A. P. K. Kutty, J. P. Malkar, M. H. Patil, Y. K. Arora, S. Sinha, P. Priya, Essy Samuel, S. Sreekumar, P. Vinod, N. P. S. Mithun, S. V. Vadawale, N. Vagshette, K. H. Navalgund, K. S. Sarma, R. Pandiyan, S. Seetha, K. Subbarao, The Cadmium Zinc Telluride Imager on AstroSat, Journal of Astrophysics and Astronomy, 38 (2017) 31.
[23] C. Erd, A. Owens, G. Brammertz, M. Bavdaz, A. Peacock, V. Lämsä, S. Nenonen, H. Andersson, N. Haack, Hard X-ray Test and Evaluation of a Prototype 32×32 Pixel Gallium–Arsenide Array, Nuclear Instruments and Methods in Physics Research A, 487 (2002) 78-89.
[24] S.M. Sze, K.K. Ng, Physics of Semiconductor Devices, 3rd ed., John Wiley & Sons, New Jersey, 2007.
[25] G. Lioliou, M.D.C. Whitaker, A.M. Barnett, High temperature GaAs X-ray detectors, Journal of Applied Physics, 122 (2017) 244506.
[26] H. Spieler, Semiconductor Detector Systems, Oxford University Press, New York, 2005.
[27] G. Bertuccio, R. Casiraghi, D. Maiocchi, A. Owens, M. Bavdaz, A. Peacock, H. Andersson, S. Nenonen, Noise Analysis of Gallium Arsenide Pixel X-ray Detectors Coupled to Ultra-Low Noise Electronics, IEEE Transactions on Nuclear Science, 50 (2003) 723-728.
[28] G. Bertuccio, P. Rehak, D. Xi, A Novel Charge Sensitive Preamplifier without the Feedback Resistor, Nuclear Instruments and Methods in Physics Research A, 326 (1993) 71-76.
[29] H. Xiaolong, Y. Shenggui, D. Chunsheng, Evaluation of the decay data of ^{109}Cd, Nuclear Instruments and Methods in Physics Research A, 621 (2010) 443-446.
[30] H.R. Verma, Measurements of M and L X-ray energies and relative intensities emanating from ^{241}Am source, Applied Radiation and Isotopes, 122 (2017) 41-46.
[31] M.-M. Be, V. Chiste, C. Dulieu, X. Mougeot, E. Browne, V. Chechev, N. Kuzmenko, F. Kondev, A. Luca, M. Galan, A.L. Nichols, A. Arinc, X. Huang, Table of Radionuclides (A=22 to A=244), Monographie BIPM-5, 5 (2010).
[32] U. Schötzig, Half-Life and X-ray Emission Probabilities of ^{55}Fe, Applied Radiation and Isotopes, 53 (2000) 469-472.
[33] G.F. Knoll, Radiation Detection and Measurements, 4th ed., John Wiley & Sons, 2010.
[34] G., Lioliou, A.M Barnett, Electronic Noise in Charge Sensitive Preamplifiers for X-ray Spectroscopy and the Benefits of a SiC Input JFET, Nuclear Instruments and Methods in Physics Research A, 801 (2015) 63-72.

[35] U. Fano, Ionization Yield of Radiations. II. The Fluctuations of the Number of Ions, Physical Review, 72 (1947) 26-29.
[36] G. Bertuccio, A. Pullia, A Method for the Determination of the Noise Parameters in Preamplifying Systems for Semiconductor Radiation Detectors, Review of Scientific Instruments, 64 (1993) 3294-3298.
[37] G. Bertuccio, R. Casiraghi, Study of Silicon Carbide for X-ray Detection and Spectroscopy, IEEE Transactions on Nuclear Science, 50 (2003) 175-185.
[38] G. Bertuccio, A. Pullia, G. De Geronimo, Criteria of Choice of the Front-End Transistor for Low-Noise Preamplification of Detector Signals at Sub-Microsecond Shaping Times for X- and γ-ray Spectroscopy, Nuclear Instruments and Methods in Physics Research A, 380 (1996) 301-307.
[39] G. Bertuccio, S. Caccia, Progress in ultra-low-noise ASICs for radiation detectors, Nuclear Instruments and Methods in Physics Research A, 579 (2007) 243-246.
[40] A. Owens, H. Andersson, M. Bavdaz, G. Brammertz, C. Erd, T. Gagliardi, V. Gostillo, N. Haack, I. Lisjutin, S.A.A. Nenonen, A.J. Peacock, H. Sipila, I. Taylor, S. Zatoloka, Development of compound semiconductor arrays for x- and gamma-ray spectroscopy, SPIE proceedings, Hard X-Ray and Gamma-Ray Detector Physics III, 4507 (2001) 42-49.